Chemical Engineering Journal 415 (2021) 127779

Contents lists available at ScienceDirect

Chemical Engineering Journal

journal homepage: www.elsevier.com/locate/cej

Pragmatically designed tetragonal copper ferrite super-architectures as advanced multifunctional electrodes for solid-state supercapacitors and overall water splitting

Vikas Sharma [a], Uday Narayan Pan [a], Thangjam Ibomcha Singh [a], Amit Kumar Das [a], Nam Hoon Kim [a,*], Joong Hee Lee [a,b,*]

[a] Department of Nano Convergence Engineering, Jeonbuk National University, Jeonju, Jeonbuk 54896, Republic of Korea
[b] Carbon Composite Research Centre, Department of Polymer-Nano Science and Technology, Jeonbuk National University, Jeonju, Jeonbuk 54896, Republic of Korea

ARTICLE INFO

Keywords:
Solid-state supercapacitors
Water-splitting
Super-architecture
Tetragonal phase
Energy devices

ABSTRACT

Stabilization of tetragonal copper ferrite super-architectures has been proposed for the fabrication of high-performance supercapacitor and water splitting electrodes. The reaction parameters are optimized to keep the tetragonal phase intact (with high yield per batch ~ 7.5 g) in order to have better ions intercalation/de-intercalation processes and longer cycling stability, according to Jahn-Teller distortion theory. The developed porous layered architectures are mesoporous with large specific surface area available for ionic interactions. The redox additive insertion in the electrolyte raises the specific capacity to ~ 450 mAh g^{-1} (~2490F g^{-1}) from the fabricated electrode. The physical mechanism involved behind the electrochemical performance in presence of redox additives is elaborately discussed to gain insight into the charge storage characteristics. The fabricated asymmetric solid-state supercapacitor exhibits broad potential window (~1.8 V) with excellent energy (128 Wh kg^{-1}) cum power traits, and a long-lasting stable performance for > 10000 cycles. For water splitting, the super-architectures based electrode displays promisingly lower OER/HER (~298/103 mV) overpotentials with excellent stability over longer durations (>30 h). The fabricated symmetric device with the alkaline electrolyte is highly stable with cell voltage of 1.62 V, which being an oxide material is excellent and superior to various oxides/chalcogenides based high-grade materials.

1. Introduction

The commercialization of energy storage and conversion devices explicitly promotes the development of eco-friendly, scalable, and cost-effective materials with large surface areas. The proportional depletion of fossil fuels with the increasing population has posed a threat to the existing energy resources. Therefore, renewable energy sources have become a center of attention, as a contemporary alternative. Emerging energy storage and generation technologies include advanced redox supercapacitors and hydrogen as fuel [1,2]. In supercapacitors, pseudocapacitive materials have shown enormous potential to boost the energy density of devices with their near-surface fast faradaic reactions [3–7]. However, these materials suffer from scalability issues because of the low yield per synthesis batch. Recently, some carbon based novel materials are also proposed exhibiting high energy density, however, their surface limited charge storage mechanism limits their energy density tenability, which can be done in case of redox materials [8–12]. H_2 generation still relies on noble electrocatalysts (Pt/C, IrO_2, and RuO_2) via water splitting, but these are also questionable for their usability at large scales [13]. Therefore, to develop cheaper and scalable alternatives, various pseudocapacitive materials including metallic/bi-metallic hydroxides, oxides, chalcogenides, phosphides and borides (specifically transition metal-based ones) have been employed owing to their multiple oxidation states, excellent electron relay system, and tunable morphologies [14–21]. Such properties make them multifunctional for redox supercapacitors as well as oxygen evolution reactions (OER) and hydrogen evolution reactions (HER).

Among the aforementioned materials, transition metal oxides (TMOs) are known to possess the maximum of the required characteristics [22–24]. Materials other than TMOs suffer from scalability and stability issues. With the development of better understanding, hierarchical structures have been found to exhibit exceptional porosity,

* Corresponding authors.
E-mail addresses: nhk@jbnu.ac.kr (N. Hoon Kim), jhl@jbnu.ac.kr (J. Hee Lee).

https://doi.org/10.1016/j.cej.2020.127779
Received 17 August 2020; Received in revised form 9 November 2020; Accepted 16 November 2020
Available online 30 November 2020

surface area, and volume for the incoming ions adsorption/accumulation [25,26]. Such structures facilitate the faradaic reactions involving fast ion adsorption/desorption for hybrid redox supercapacitors [27]. In addition, their equal effectiveness has been observed for HER/OER reactions, which reduces the complexity of having catalytic systems involving loathsome strategies to use different electrodes for HER and OER, in alkaline solutions [28]. In TMOs, spinels are effective hosts because of their bi-metallic nature with tunable morphologies [29]. $CuFe_2O_4$, an inverse-spinel, exhibits stupendous theoretical specific capacity (~895 mAh g^{-1}) and reasonably good electrical conductivity because of its low bandgap (~1.9 eV) [17,30]. Given the Jahn-Teller effect, the tetragonal phase of $CuFe_2O_4$ is relatively stable at lower temperatures and gets transformed to the cubic phase at elevated temperatures, depending on the synthesis approaches utilized [31–34]. The cubic phase experiences Jahn-Teller distortions, which limits their long-term phase stability as electrodes. Cu^{2+} is a Jahn-Teller cation here, which in tetrahedral coordination leads to a tetragonal phase with constricted dimensions effective for providing directional pathways to the incoming ions [31]. To the best of our knowledge, there has been no report before on layered porous super-architectures of tetragonal $CuFe_2O_4$ (stable even at 500 °C), with a high yield per batch, as multifunctional material for energy storage and conversion applications.

The present work reports a novel rational approach for designing hierarchical porous super-architectures of tetragonal $CuFe_2O_4$ (*t*-CuF_500) that exhibit perfect phase crystallinity even at 500 °C. The evolution of layered hierarchical structures and increased porosity provides ample volume for adsorption/desorption of incoming ions to achieve high specific capacity. The specific capacity is further modulated to three fold by inserting a redox additive into the host electrolyte in optimized amounts. For full device fabrication, a redox-gel electrolyte is used to eliminate the issues related to electrolyte leakage, handling, short-circuiting, and conductivity [35]. The fabricated ~ 1.8 V solid-state asymmetric supercapacitor (ASC) with a rare combination of carbon nanotubes and carbon black based negative electrode exhibits sparklingly high energy and power densities with stable performance for > 10,000 cycles. For water splitting, the super-architecture exhibits a superior performance for OER and HER with reasonably lower overpotentials, along with exceptionally good stability for > 30 h. The strategy, as shown in Scheme 1, establishes a facile scalable approach to achieve high performance integrated energy storage and conversion systems.

2. Materials and methods

2.1. Chemicals required

Copper acetate monohydrate ($Cu(C_2H_3O_2)_2{\cdot}H_2O$), ferric nitrate nonahydrate ($Fe(NO_3)_3{\cdot}9H_2O$) oxalic acid ($C_2H_2O_4$) and ethylene glycol were procured from Sigma Aldrich for the materials synthesis. Functionalized multi-walled carbon nanotubes (CNTs) and potassium ferricyanide (PFCN) were also purchased from Sigma Aldrich. The precursors were used as purchased without further purification. For the electrochemical measurements, polyinylidene fluoride, carbon black (CB) and N-methyl-2 pyrrolidone (NMP) were procured from Samchun Chemicals.

2.2. Synthesis of materials

The synthesis process was optimized by tuning the obtained precursor at various temperatures to achieve super-architectures with the desired tetragonal phase of $CuFe_2O_4$. The facile synthesis protocol to obtain the precursor Cu-Fe hydroxide powder involved preparation of a solution containing 2 g of $Cu(C_2H_3O_2)_2{\cdot}H_2O$ and 8 g of $Fe(NO_3)_3{\cdot}9H_2O$ in 35 ml ethylene glycol and 15 ml de-ionized (DI) water. The solution was ultra-sonicated for 15 mins to obtain a clear solution then 3.5 g of $C_2H_2O_4$ was added to the as-prepared solution and stirred for 30 mins to achieve a uniform solution. The obtained solution was sealed in a Teflon-lined stainless-steel autoclave kept at 120 °C for 24 h. After cooling to room temperature, the powder was separated out by centrifugation and washed subsequently with DI water and ethanol many

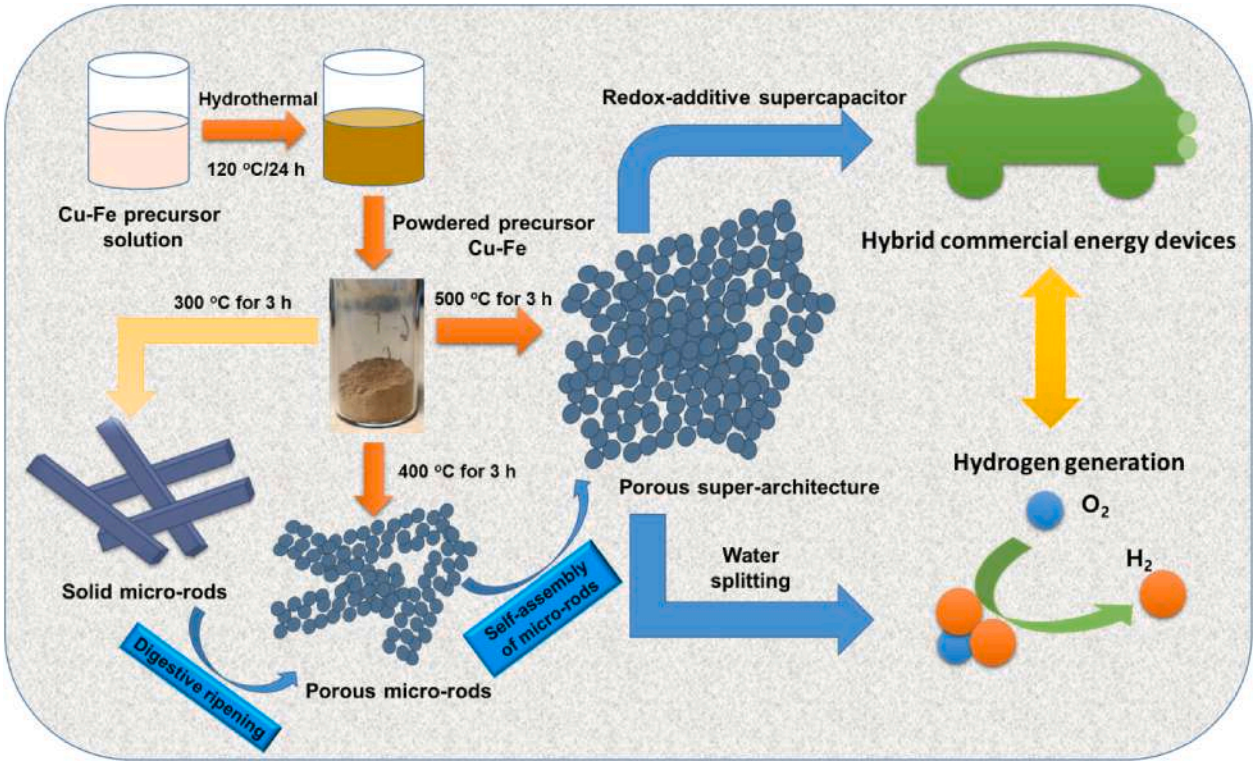

Scheme 1. Schematic representation of the strategies used to achieve multifunctional *t*-CuF_500 for high performance supercapacitorand water splitting electrodes.

times, until the neutral pH was achieved. The collected powder was then dried overnight at 60 °C in the oven, under air atmosphere. The obtained yield of the precursor powder was found to be ~ 10 g in one batch. To see the effect of temperature, the obtained precursor was divided into three parts and separately annealed in air at 300 °C, 400 °C and 500 °C for 3 h with a ramp rate 1 °C/min, in air. Color transition was observed in the powder from light brown to dark brown indicating towards the formation of oxide phase.

2.3. Materials characterization

The phase identification of the synthesized materials was performed by analyzing the XRD profilesobtained using Rigaku Corporation, Tokyo, Japan. The morphology identification was performed by FE–SEM (SUPRA 40 VP; Carl Zeiss, Germany). The intrinsic morphological characteristics, diffraction rings and SAED patterns were collected using HRTEM (H–7650; Hitachi Ltd., Japan). The oxidation states of the respective ions in the material were identified by analyzing the XPS (Theta Probe; Thermo Fisher Scientific, UK) profiles. The Fourier transform infrared (FT-IR) spectroscopy measurements were performed using PerkinElmer spectrophotometer (Spectrum two, UK) following the KBr pellet method. The elemental compositions of the as-obtained electrode materials were investigated by energy dispersive X-ray analysis (EDAX, SUPRA 40 VP; Carl Zeiss, Germany). Surface area and pore size measurements were done by analyzing the N_2 adsorption–desorption isotherms collected using Micromeritics ASAP 2020 surface area analyzer operated at 77 K, for the synthesized materials.

2.4. Electrochemical measurement (Supercapacitors)

Electrochemical characterization of the synthesized materials was performed initially using a three-electrode configuration equipped with Ag/AgCl and Pt electrode as the reference and counter electrodes, respectively, in 2 M KOH aqueous electrolyte solution. Slurries for the working electrodes were prepared with 80 wt% of the active material (synthesized materials i.e. *t*-CuF_300, *t*-CuF_400 and *t*-CuF_500), 10 wt% of carbon black, and 10 wt% of polyvinyldienefluoride (as binder). All the components were integrated together using NMP as mixing media. The obtained slurry was drop casted onto a pretreated Ni foam (with 30 wt% HCl, water and acetone washed) with dimension 1 cm × 1 cm. Similarly, in the presence of redox additive, different compositions i.e. 0.01 M, 0.02 M and 0.03 M of PFCN were inserted into the host electrolyte. For negative electrodes measurements, similar process was followed for the fabrication of the respective electrodes. The negative electrode materials were optimized by using three configurations in wt %; (i) CNT_{100}, (ii) CNT_{50} + CB_{50} and (iii) CB_{100}, respectively. The fabricated electrodes were characterized using cyclic voltammetry (CV), galvanostatic charge–discharge (GCD) and electrochemical impedance spectroscopy (EIS) on CHI660E potentiostat. EIS measurements were performed in the frequency range of 0.01 Hz to 100 kHz.

Device fabrication was accomplished by assembling *t*-CuF_500 as positive electrode and CNT_{50} + CB_{50} as negative electrode. Cellulose paper was sandwiched in between the electrodes as separator to avoid short-circuiting. The electrodes were square in shape with size ~ 1.5 cm^2. Electrodes were prepared in the same way as done in case of three electrode measurements by optimizing the mass to charge ratio for both the materials (discussed in supporting information). Here, the gel electrolyte was used to fabricate a solid-state asymmetric supercapacitor. The ratio of PVA and KOH was kept 1:2 for PVA:KOH gel electrolyte and for redox-gel electrolyte i.e. PVA:KOH:$K_3Fe(CN)_6$, the enetities were kept in 1:2:0.02 ratio. The observed results using CV, CD and EIS measurements were carefully analyzed and discussed in the paper.

2.5. Water splitting measurements

The electrocatalytic activities of NF, *t*-CuF_500/NF, RuO_2/NF and Pt/C/NF for OER, HER, and overall water splitting were analyzed on a CHI 660E electrochemical workstation using three-electrode (for OER and HER) and a two-electrode system (for overall water splitting). The electrodes of dimensions 1 cm^2 with mass loading ≈5mg cm^{-2} were used as working electrodes. A graphite rod and Ag/AgCl (in 3 M saturated KCl) were used as counter and reference electrodes, respectively. Freshly prepared aqueous 1.0 M KOH solution was used as electrolyte for the measurements. Electrochemical impedance spectroscopy (EIS) measurements were performed by supplying an AC voltage of amplitude 5 mV in the particular frequency range of 0.01 Hz–100 kHz. All the potentials were changed to RHE using the Nernst equation ($E_{RHE} = E_{Ag/AgCl} + 0.059 \times pH + 0.197$). The LSV curves were iR-corrected by using the equation $E_C = E_M$ - iR_C, where R_C, E_M and E_C represent the corrected resistance, experimentally obtained potential and iR-corrected potential, respectively. The overpotential (η) values were obtained from the equation $\eta = E_{RHE}$-1.23 V. For comparison, commercial Pt/C (20 wt%) and RuO_2 (99.9 wt%, Alfa) were loaded on a 1 cm^2 area of pre-cleaned NF. The catalyst's inks were made by dispersing Pt/C and RuO_2 (5 mg) separately in a solution mixture of isopropyl alcohol (750 μL), DI water (200 μL), and nafion (50 μL) for 30 min under ultra-sonication[36].

2.6. Mathematics involved

The gravimetric capacitances from the CV profiles in the three electrode configuration were calculated using the relation[27]:

$$C_{CV} = \frac{1}{2mVs}\int_{-V}^{+V} I.dV \tag{3}$$

where C_s, I, m, V, *s* represent the gravimetric capacitance in F g^{-1}, the current generated at a certain potential in ampere (A), the mass of the active material in gram (g), potential window in volts (V) and scan rate in V s^{-1}, respectively.

On the other hand, the gravimetric capacitances from the charge discharge profiles were calculated using[27]:

$$C = \frac{I.dt}{m.dV} \tag{4}$$

where I/m, dt and dV denote current density in A g^{-1}, discharge time in seconds (s) and potential window in volts (V), respectively. For the device related calculations, charge discharge curves were considered and the same relation mentioned in eq. (3) was utilized.

The specific capacity (C_S, in mAh g^{-1}) of the electrodes in three-electrode configuration and the ASC device were calculated using [37]:

$$C_S = \frac{2I\int V.dt}{mV} \tag{5}$$

The asymmetric supercapacitor was fabricated by balancing the charge to mass ratio for both the negative and positive electrodes using the relation[37]:

$$\frac{m_+}{m_-} = \frac{\Delta V_- C_-}{\Delta V_+ C_+} \tag{6}$$

where C_- and C_+ are the gravimetric capacitances (in F g^{-1}) measured at the same scan rate, using the three electrode system, for negative and positive electrodes, respectively while ΔV_+ and ΔV_- denote the working potential window for the positive and negative electrodes, respectively.

The energy and power density of the fabricated asymmetric supercapacitor were calculated as per the relations mentioned below[37]:

$$E = \frac{1}{2*3.6}CV^2 \tag{7}$$

$$P = \frac{E}{t}*3600 \tag{8}$$

where E, P, C, V, t represent energy density in Wh kg^{-1}, power density W kg^{-1}, capacitance of device in F g^{-1}, voltage window in volts (V) and discharge time of device in seconds (s), respectively.

3. Results and discussion

A facile hydrothermal synthesis strategy followed by post-annealing was used for the materials synthesis. Fig. 1**A** shows the XRD profiles of the synthesized materials annealed at different temperatures (i.e. 300 °C (*t*-CuF_300), 400 °C (*t*-CuF_400) and 500 °C (*t*-CuF_500)). The observed XRD profiles were matched with JCPDS card no.: 34–0425 representing the I 4_1/amd space group and confirmed the tetragonal phase of $CuFe_2O_4$.[34] On careful investigation, it was found that the peak intensities were significantly increased at elevated temperatures, and the undiscernible peaks (such as (202), (312) and (321)) in *t*-CuF_300 become distinguishable in *t*-CuF_500. The peak for the (202) plane was reduced and the (211) plane became more intense showing the improvement in the material's crystallinity at elevated temperatures, without phase distortion. In addition, the peak width was reduced with

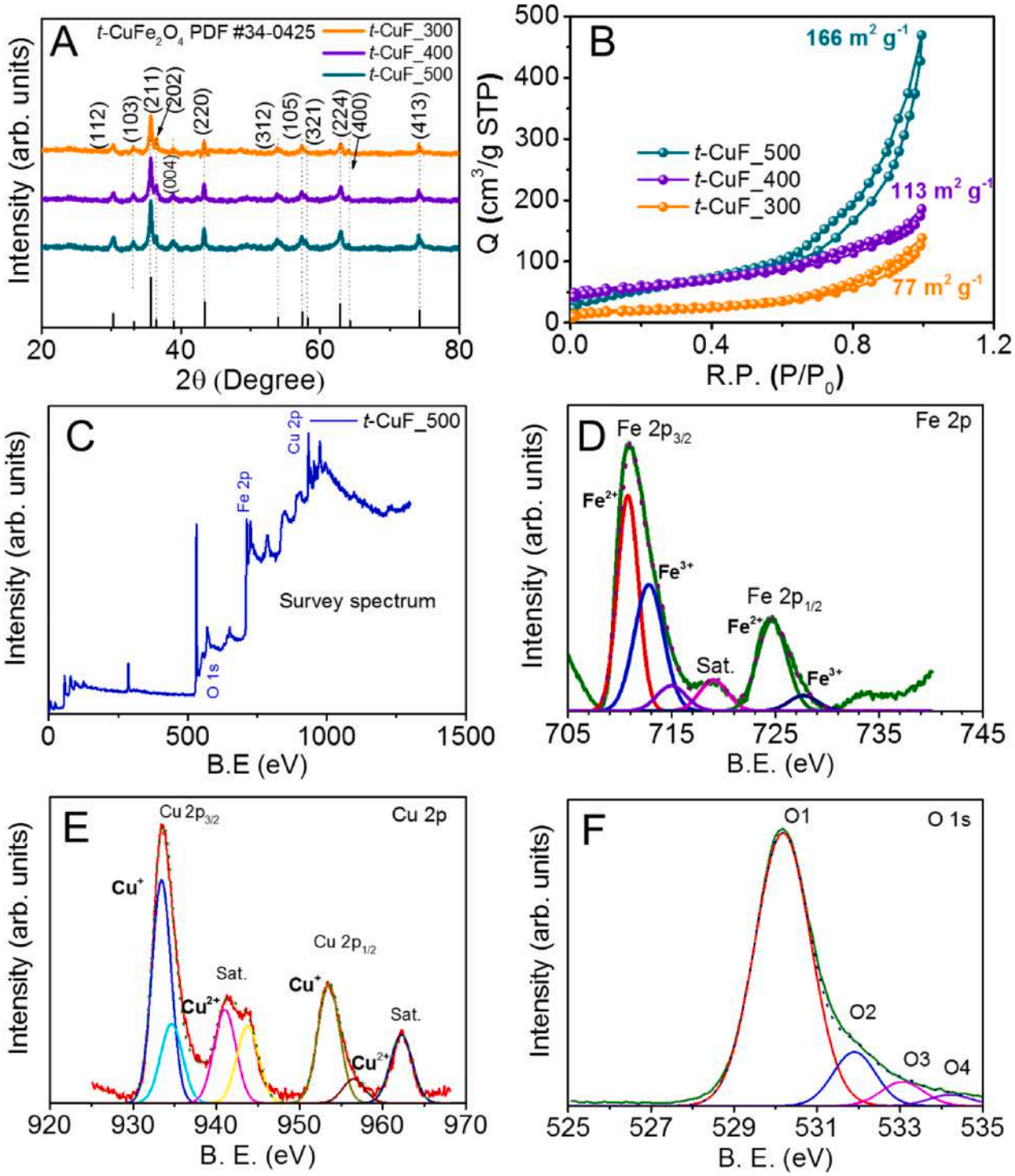

Fig. 1. (A) XRD profiles, (B) N_2 adsorption–desorption isotherms for *t*-CuF_300, *t*-CuF_400 and *t*-CuF_500, respectively, and (C-F) XPS profiles including survey spectrum and related to respective elements in *t*-CuF_500.

temperature, from 0.31 to 0.28 nm (for the (220) plane at 35.73°), confirming the crystallite size transition (see Fig. S1). Fourier transform infrared (FTIR) spectroscopy profiles for the synthesized materials, as shown in Fig. S2, confirmed the presence of Cu–O/Fe-O bonds at ~ 431 and ~ 592 cm^{-1}, respectively, corresponding to the tetrahedral and octahedral sites in the spinel structure with no discernible impurity peak. Two other peaks that evolved at ~ 1640 and ~ 2360 cm^{-1} could be assigned to the stretching and bending modes of water molecules, respectively.[38]

Phase transformation of the as-prepared hydroxide to the respective tetragonal and cubic oxides was cross-confirmed by analyzing the thermo gravimetric profile, as shown in Fig. S3. It is clearly depicted from the profile that the phase transformation from hydroxide to oxide was started after 200 °C and it was fully converted to *t*-CuF at ~ 250 °C. The tetragonal phase remained stable till 500 °C and after that it converted to cubic $CuFe_2O_4$ at ~ 580 °C. The N_2 adsorption–desorption isotherms, as shown in Fig. 1**B**, depicted a progressive increase in the specific surface area as *t*-CuF_300 (77 $m^2 g^{-1}$) < *t*-CuF_400 (113 $m^2 g^{-1}$) < *t*-Cuf_500 (166 $m^2 g^{-1}$), maintaining the shape in accordance with type IV adsorption isotherm, thus confirming the mesoporous nature of the materials.[27] The improvement in the adsorption characteristics was also evidenced from the Barrett, Joyner, and Halenda (BJH) pore size distribution profiles, as shown in Fig. S4. With the effective increment in pore diameter along with surface area (~5.58 to ~ 8.18 nm, the Fig. shows pore radius), a synergistic enhancement in the materials adsorption/desorption characteristics was anticipated. High-resolution X-ray photoelectron spectroscopy (XPS) measurement was performed for *t*-CuF_500, as shown in Fig. 1**C-F**. The presence of Fe 2p (~711/724 eV), Cu 2p (~934/944 eV), and O 1 s (~532 eV) related spectra with deconvoluted peaks were perfectly consistent with the literature for the stable tetragonal phase of $CuFe_2O_4$. A small peak that emerged at ~ 718 eV could be assigned to the presence of Fe^{3+} ions in the lattice[39].

Further, the morphological investigation was performed by analyzing the scanning electron microscopy (SEM) and transmission electron microscopy (TEM) micrographs as shown in Fig. 2**A**-G. Transitions in morphology with temperature were observed from solid micro-bars (300 °C) to porous micro-bars (400 °C) to micro-bars assembled in hierarchical, layered, and porous super-architectures (500 °C, see Fig. S5**A-C**). The particles size was also increased with the increase in calcination temperature, which was evident from XRD

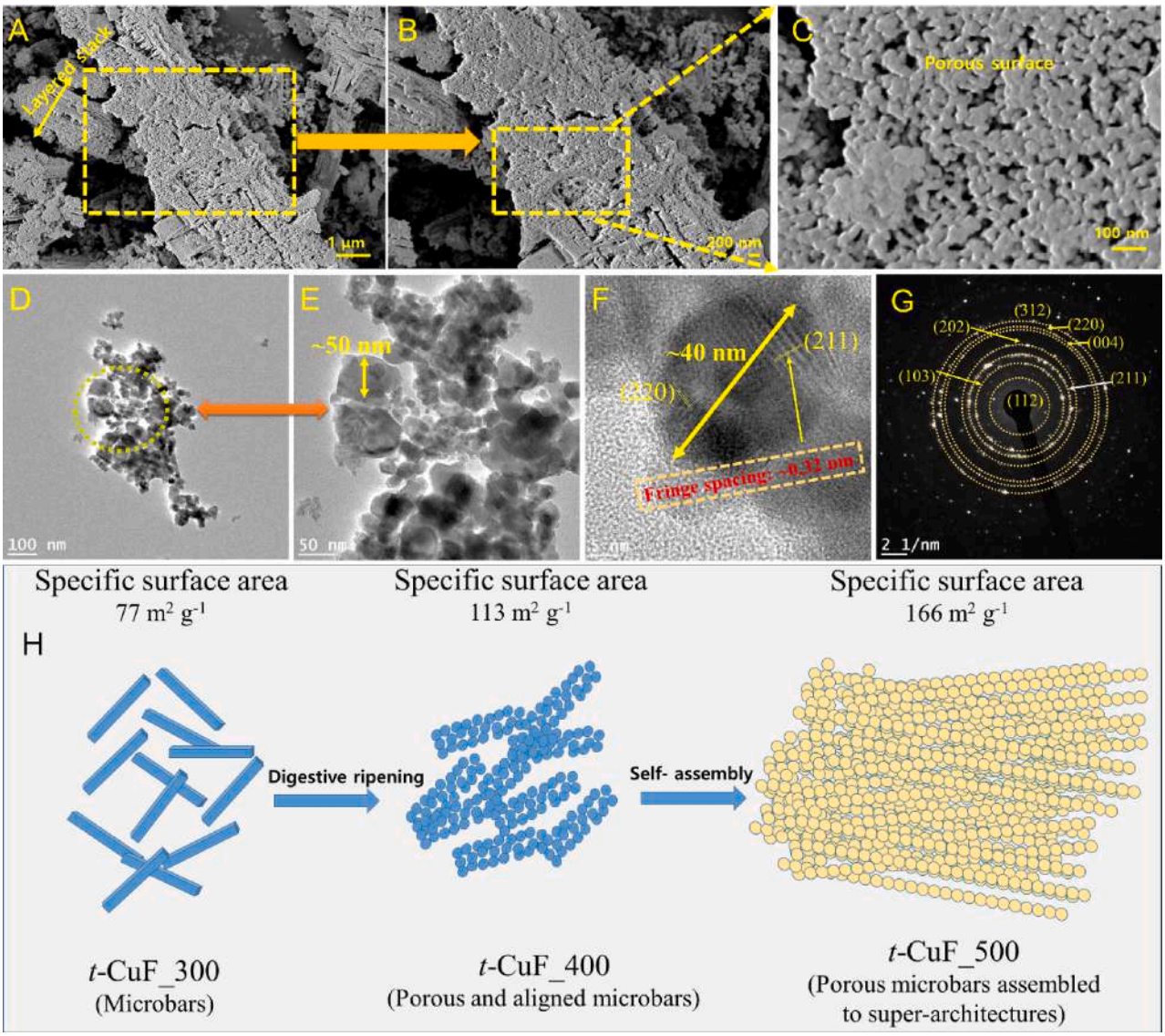

Fig. 2. (A-C) SEM micrographs at low and high magnifications, (D-E) TEM micrographs at 100 and 50 nm scales, (F) HRTEM micrographs exhibiting the fringe patterns, (G) diffraction patterns for *t*-CuF_500, and (H) morphology evolution schematic representation giving the underlying phenomena involved with the elevation of temperature.

profiles where the peak width was reduced indicating towards increment in crystallite size. Precisely, it is well known that at higher temperatures samples become more condensed which leads to evolution of aligned structures in the direction of minimization of surface energy. Initially at 300 °C, microbars with solid external surface were evolved as the growth mechanism favored the 1-D assembly and growth of the evolved nanoparticles. With the increase in the calcination temperature, the solid bars transformed into porous micro-bars following the digestive ripening mechanism. During the digestive ripening, small particles started to evolve from the solid surface where the charged particles' electrostatic energy acts as a complementing force alongside the curvature generating layers in the solid structure [40]. These porous layered bars, later at 500 °C, condensed and assembled to stabilize the hierarchical micro-bed like super-architectures in order to minimize their edge and surface energies (as shown in Fig. 2**A-E**). Such assembly led to the development of pores in the structure with the evolution of layers, which would be responsible for the enhanced ionic interaction during the electrochemical processes (discussed later). Fig. 2**F** shows the fringe pattern observed on a single particle with size ~ 40 nm; the fringe width was ~ 0.32 nm. The diffraction pattern for *t*-CuF_500, as depicted in Fig. 2**G**, shows a clear planar view from the rings observed at the submicron level which could be designated to the corresponding planes

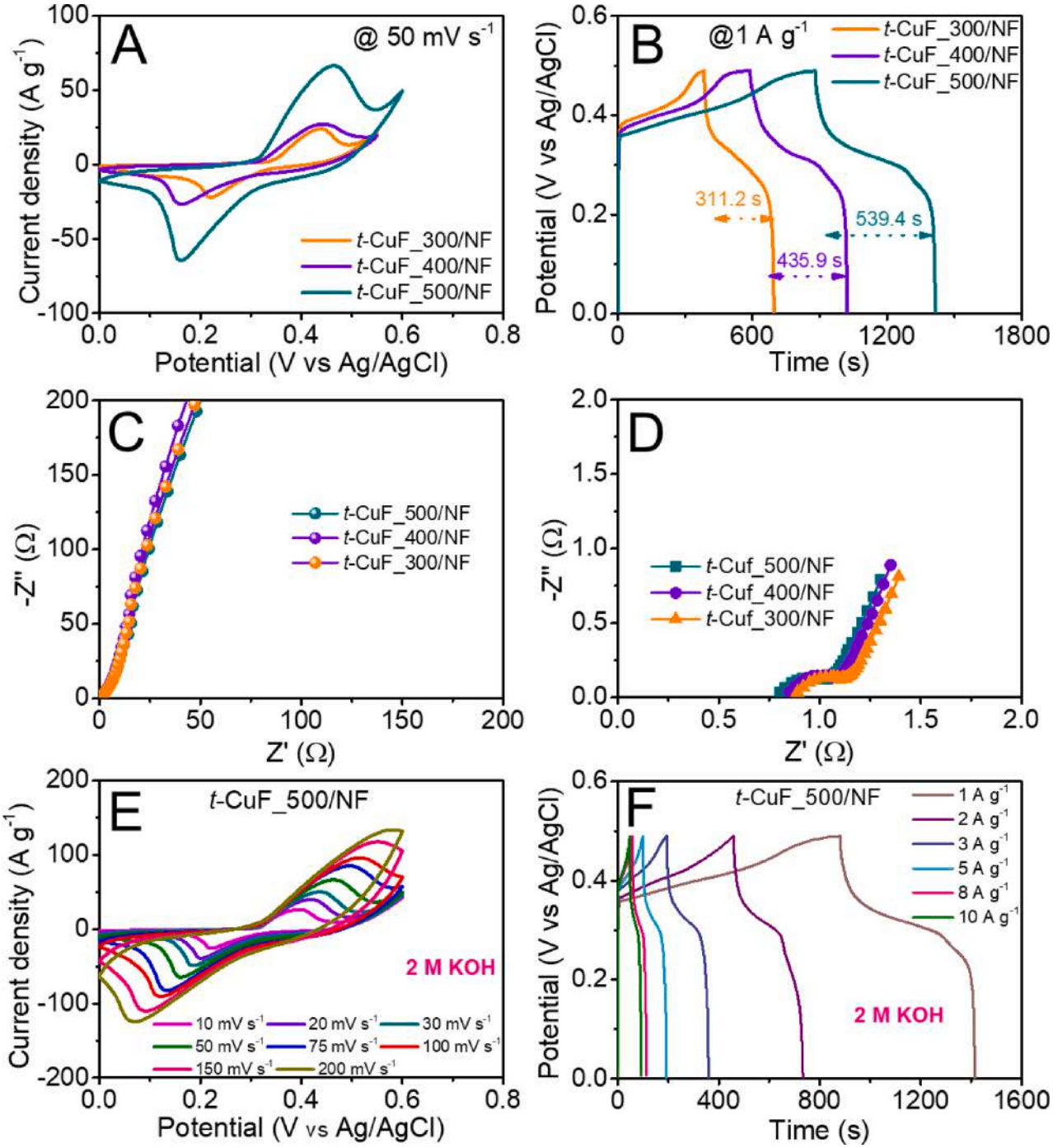

Fig. 3. Electrochemical characterization in three electrode configuration; (A) CV profiles @50 mV s^{-1}, (B) CD profiles @1 A g^{-1}, (C) EIS profiles for *t*-CuF_300/NF, *t*-CuF_400/NF and *t*-CuF_500/NF, respectively, (D) the high frequency region of EIS profiles showing R_{CT} and R_S, (E) CV profiles at various scan rates, and (F) CD profiles at different current densities in 2 M KOH for *t*-CuF_500/NF.

observed in the XRD profile. The elemental mapping and their respective contributions (Energy dispersive spectroscopy) are also shown in **Fig. S6 and S7,** and **Table S1** exhibits good distribution of the respective elements in the super-architecture. The morphology evolution showing the growth mechanism is schematically represented in Fig. 2**H.**

3.1. Electrochemical characterizations for supercapacitor

The three-electrode measurements were performed in 2 M KOH aqueous electrolyte. $CuFe_2O_4$ generally exhibits the faradaic transition in an alkaline electrolyte within a positive potential range as per the following reaction:[41]

$$CuFe_2O_4 + H_2O + 2e^- \leftrightarrow CuO + 2FeO + OH^- \quad (1)$$

The redox reactions originated because of the inter-valence charge transfer between Cu^{2+}/Cu^{+} and Fe^{3+}/Fe^{2+} redox couples. Fig. 3**A** compares the cyclic voltammograms (CV) observed at 50 mV s^{-1} for three different electrode materials. Among them, *t*- CuF_500 exhibited the maximum current density and enclosed area with a slightly high potential window of ~ 0.6 V (the other two, ~0.55 V). Further, the

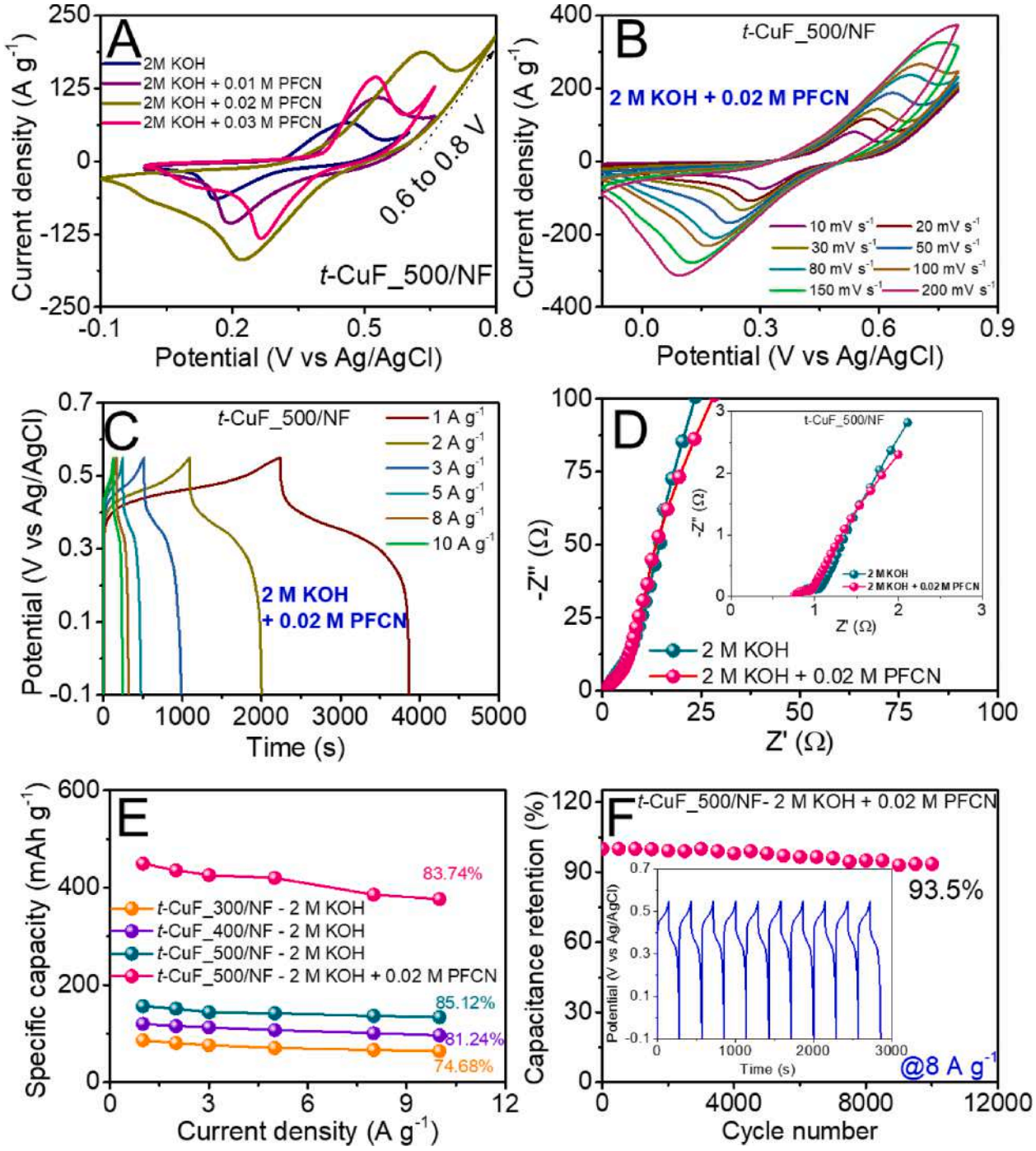

Fig. 4. (A) Comparative CV profiles @50 mV s^{-1} at different redox additive concentrations for *t*-CuF_500/NF, (B-C) CV and CD profiles at different scan rates and current densities in 0.02 M PFCN for *t*-CuF_500/NF, (D) EIS profiles in the absence and presence of the redox additive (inset shows the high frequency region), (E) variation of specific capacity with current density for different electrodes and optimized redox additive based configuration, and (F) Cycling performance for *t*-CuF_500/NF in the presence of redox additive (inset displays last ten cycles) at 8A g^{-1}.

galvanostatic charge–discharge (GCD) profiles recorded at 1 A g^{-1} also cross-verified the CV results, as shown in Fig. 3**B**. The EIS profiles (Fig. 3**C-D**) revealed information about the charge storage kinetics at the electrodes and specified that the increment in surface area and transition from solid bars to assembled super-architectures led to a consistent decrease in equivalent series resistance (R_S) and charge transfer resistance (R_{CT}) from ~ 0.89 Ω to ~ 0.82 Ω and ~ 1.14 Ω to ~ 1.07 Ω, respectively. To estimate the specific capacity and rate capability of the electrodes, CV and GCD profiles were taken at various scan rates (10–200 mV s^{-1}), and current densities (1–10 A g^{-1}), respectively, as shown in Fig. 3**E,F and S8, S9**. On comparison, it was proved that the super-architectures based electrode with enhanced surface area and layered morphology paved way for more ions at the electrodes which led to a high enclosed area of the CV profiles in comparison to the other two. To confirm the phase directed electrochemical performance control in $CuFe_2O_4$, the precursor annealed at 600 °C was also characterized using XRD and later investigated in three-electrode cell configuration. The observed XRD profile depicting the formation of cubic $CuFe_2O_4$ (*c*-CuF_600) phase along with comparative CV profiles (@50 mV s^{-1}) for *c*-CuF_600 and *t*-CuF_500 are shown in **Fig. S10A-B**. The observed results clearly exhibited the superiority of tetragonal phase over cubic phase in electrochemical performance.

The electrolyte tuning state of the art using redox additives is a novel concept. The redox additive reduces the chemical potential required for the reactions and thus, synergistically contribute in the reaction processes to improve the electrode performance. Here, potassium ferricyanide (PFCN) with different molar concentrations viz., 0.01 M, 0.02 M and 0.03 M were tested in the host electrolyte for *t*-CuF_500/NF. Fig. 4**A** shows the change in the CV profiles collected at 50 mV s^{-1} for *t*-CuF_500 based electrodes with the addition of PFCN. The enclosed CV area was increased along with the potential window. The presence of the redox couple $Fe(CN)_6^{3-}/Fe(CN)_6^{4-}$ increased the effective collected charge at the electrode. The optimum concentration in this case was 0.02 M PFCN, which exhibited a ~ 0.9 V potential window, as depicted from the CV profiles. Beyond this, the window along with the enclosed CV area was reduced because of the inter-ionic repulsions generated by excessive ions accumulation leading to under-utilization of the active surface sites. The CV and GCD profiles for the optimized configuration at various scan rates and current densities are shown in Fig. 4**B, C**. Comparative CV and GCD profiles of electrodes with and without a redox additive (optimized concentration i.e. 0.02 M PFCN) at 1 A g^{-1} are shown in **Fig. S11 and S12**.

Quantitatively, the maximum specific capacity for *t*-CuF_500/NF in 2 M KOH was ~ 160 mAh g^{-1} at 1 A g^{-1}, whereas the same was ~ 125 and ~ 90 mAh g^{-1} for *t*-CuF_400 and *t*-CuF_300, respectively (Fig. 4**D**). The mathematical equations used for the quantitative evaluation of electrodes and device are discussed in the supporting information. The calculated values of gravimetric capacitance and specific capacity at various current densities are listed in **Tables S2 and S3**, respectively. The layers and porosity evolution at elevated temperatures increased the charge space and lowered the diffusion coefficient for the incoming ions, which provided more active sites to be accessed in the super-architectures. **Table S4** shows the superiority of the present gravimetric capacitance values over some recently reported results. To date, the present values are the highest, to the best of our knowledge, reported in case of copper ferrites. Moreover, the rate capability was excellent for the *t*-CuF_500 based electrodes with capacitance retention of ~ 85% at 10 A g^{-1} (Fig. 4**D**). The maximum specific capacity was increased to ~ 450 mAh g^{-1} at 1 A g^{-1}, about three-fold that of the value observed in 2 M KOH. **Fig. S13** compares the specific capacity for all configurations where the rate capability of the redox-additive based system was excellent with ~ 84% capacity retention. The increased specific capacity values were also supported by the EIS results (Fig. 4**E**), where the R_S and R_{CT} values were reduced to ~ 0.73 Ω and ~ 0.94 Ω, respectively, along with the emergence of Warburg characteristics. A bar chart representing R_S and R_{CT} values changes with the different configurations is shown in **Fig. S14**.

The coulombic efficiencies for the electrodes are plotted in **Fig. S15**, which were maximally stable in the redox additive based configuration with few fluctuations (>70%), because of the balanced redox reactions occurring even at high current densities that are necessary to maintain effective charge accumulation and release. Thus, the power drawn remained balanced with energy stored at the electrode. Fig. 4**F and S16** show the cycling stability for *t*-CuF_500 in 2 M KOH and 2 M KOH + 0.02 M PFCN performed at 8 A g^{-1}; the capacitance retention values were ~ 91% and ~ 94%, respectively. The peak current vs scan rate curves for all the four configurations are shown in Fig. 5**A-D**, proving quasi-reversibility of all the electrodes, as linear increment in the current was observed with the increment in the scan rate across the electrodes. The redox additive based electrodes, even though experiencing high number of redox reactions in comparison to the other configurations, due to their high surface active sites and excellent charge transfer mechanism were able to show equivalent reversibility as the electrodes without redox additive.

Diffusive and capacitive contributions were measured by deconvolution of CV profiles using the power law i.e. $i = av^b$, where v represents the scan rate; 'a' and 'b' are adaptable parameters. Generally, $b = 1$ for the capacitive process, whereas $b = 1/2$ for an ideal diffusion-limited faradaic process, which satisfies Cottrell's equation: $i = av^{1/2}$. [42] The curve in **Fig. S17** shows the increment in diffusion-limited contribution with the morphology tuning first and later by electrolyte tuning sequentially. Such behavior was expected with the insertion of redox additive into the host electrolyte and it led to enhancement in the observed specific capacity.

For the fabrication of a full device, we optimized the anode material by mixing multiwalled-CNTs and carbon black in an optimum amount. The SEM micrographs of as purchased MWCNTs, carbon black and CNT_{50} + CB_{50} powders are shown in **Fig. S18A-F**, respectively. The results shown in **Fig. S19A-C** proved that the configuration CNT_{50} + CB_{50} (carbon nanotubes 50 wt% and carbon black 50 wt%) was best with 176 F g^{-1} gravimetric capacitance at 30 mV s^{-1} (see **Fig. S19D**). It is well known that composites fabricated by mixing two competent phases can lead to enhancement in properties. Similar to this, in the present case, 1D CNTs when clubbed with CB particles led to increment in charge collection at the electrodes, where CNTs provided directed pathway and carbon black actied as charge concentrators. Additionally, the CNTs bind the CB particles together, and the mechanical strength of composites increased greatly and which also increased the composite conductivity as observed from the CV profiles with enhanced size of the loop. Fig. 6**A** shows the CV profiles exhibiting the expected potential window from the devices in optimized electrolytes. Two solid-state ASCs were fabricated, namely, (i) CNT_{50}-CB_{50}||*t*-CuF_500 in PVA_KOH and (ii) CNT_{50}-CB_{50}||t-CuF_500 in PVA_KOH + PFCN. **Fig. S20** shows the potential window optimization for the solid-state ASC in PVA_KOH gel electrolyte (ASC_PVK), which was stable up to ~ 1.5 V (shorter than expected (V_{exK}) ~ 1.6 V, explained later). The CV profiles, at various scan rates, are shown in Fig. 6**B**, which proved the good reversibility of electrodes at higher scan rates. The GCD profiles at different current densities, as shown in Fig. 6**C**, evidently replicate the CV profiles with excellent charge storage characteristics.

Further, we fabricated a hybrid solid-state asymmetric supercapacitor with PFCN redox additive (ASC_PVKP). The CV and GCD profiles exhibited the increased enclosed area and the discharge time, respectively, as shown in Fig. 6**D, E**. Moreover, the expected potential window i.e. 1.8 V was fully accessible without compromise. The CV and GCD profiles showed excellent symmetry exhibiting nearly ideal capacitive characteristics, because of the balanced ionic transportation and equilibrium generated at both the electrodes with their repetitive redox reactions. A schematic of the configuration is shown in Fig. 6**F**. The maximum specific capacity from ASC_PVKP was 142 mAh g^{-1}, contemporary to the ASC_PVK which was ~ 63 mAh g^{-1} (see Fig. 6**G**).

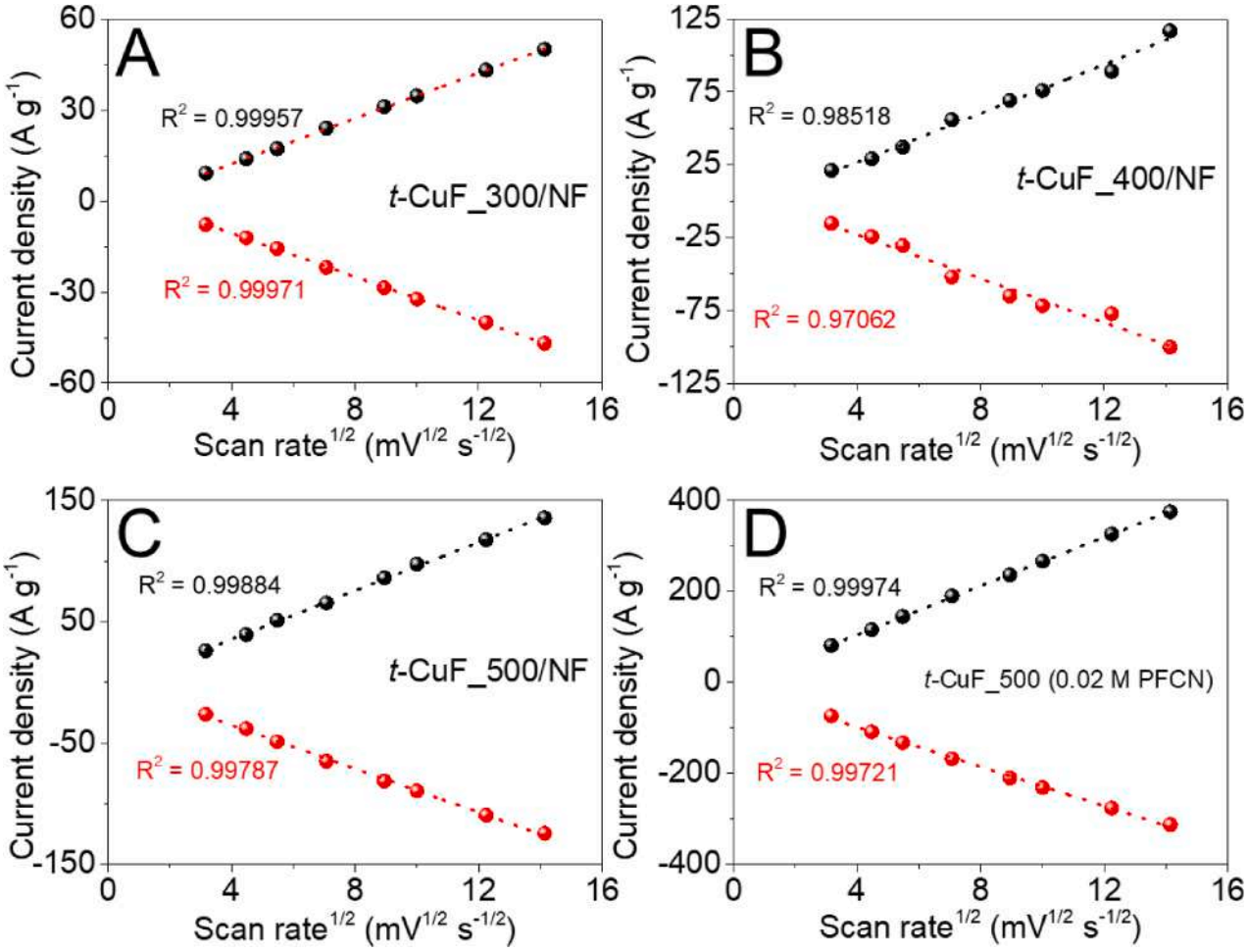

Fig. 5. (A-D) Variation of anodic and cathodic peak currents with square root of the applied scan rates for different electrodes in absence and presence of redox additive.

Variation of gravimetric cell capacitance and cell capacity with current density are shown in Fig. S21 and S22 and the corresponding values are listed in **Table S5**. The excellent capacity retention of ~ 78% was observed for ASC_PVKP at 10 A g^{-1} proving the excellent rate capability of the fabricated supercapacitor. The coulombic efficiency for the redox-additive-based device was ~ 80%, whereas it was ~ 68% for the device without redox-additive, at 1 A g^{-1}, as visible in Fig. S23. Fig. 6**H** shows the ragone bar plot for the ASC_PVKP which exhibited breakthrough energy density of ~ 128 Wh kg^{-1} with an excellent power density of ~ 900 W kg^{-1} (at 1 A g^{-1}). These values were ~ 47 Wh kg^{-1} and ~ 750 W kg^{-1} for ASC_PVK. Even at 10 A g^{-1}, the ASC_PVKP exhibited an energy density of ~ 100 Wh kg^{-1} (power density ~ 8300 W kg^{-1}), which was more than three times that of the ASC_PVK i.e., ~32 Wh kg^{-1} (power density ~ 9400 W kg^{-1}), proving the excellent power capability of the device (inset shows two red LEDs lit by two devices connected in series). The Ragone plot for ASC_PVK is shown in Fig. S24 and the values of energy and power densities for both devices at various current densities are listed in **Table S6**. The cycling performance, as shown in Fig. 6**I**, proved the excellent repeatability for the devices, where ASC_PVKP and ASC_PVK showed ~ 95% and ~ 91% capacitance retention after 10,000 cycles at 10 A g^{-1}, respectively. The EIS profiles, shown in Fig. S25 and S26, for ASC_PVK and ASC_PVKP before and after 10,000 cycles further confirmed the superior charge-storage kinetics and interfacial electrochemistry in the presence of redox-gel electrolyte. The lower values of R_S (~0.94 Ω) and R_{CT} (~1.02 Ω) along with the reduced semicircle in ASC_PVKP confirmed the observed results, and the same was sustained after cycling also, confirming the excellent stability of the fabricated device. A comparison of present results with some recently reported results on supercapacitors is shown in **Table S7**.

The charge storage mechanisms occurring in the devices are shown in Fig. 7. The effective cell window can be represented by:[43]

$$E = \frac{(\Phi_n - \Phi_p)N_A}{F} + \Delta P_1 + \Delta P_2 \quad (2)$$

where Φn/Φp are the work functions for negative/positive electrodes, N_A and F represent the Avogadro's number and Faraday constant, respectively; and ΔP_1 and ΔP_2 are the respective electrode potentials for negative and positive electrodes. Two factors govern the maximum operating voltage window in any ASCs; these are: (i) ΔΦ (i.e., Φn − Φp) and (b) solvent decomposition energy. As per the relative band gaps of the electrode materials, the work function difference is near to 2 eV. Therefore, the optimum voltage window for the device should ≤ 2 V, theoretically (as per equation (2)). The chemisorption of H^+/OH^- ions at the negative/positive electrodes modifies the electrode work function and reduces the maximum achievable potential.[44] Here comes the role of electrolyte support to the achievable potential window. If the electrolyte ions provide sufficient balance to the electron transfer process to the electrodes then the maximum offered potential window can be achieved. In ASC_PVK based device, the maximum observed potential was ~ 1.5 V, which was actually less than the expected ~ 1.6 V. On the other hand, the involvement of additional redox ions because of the $Fe(CN)_6^{3-}/Fe(CN)_6^{4-}$ couple led to an increase in the dissociation constant of the electrolyte, which consequently let the electrolyte sustain a high voltage up to ~ 1.8 V. These physical phenomena improved the

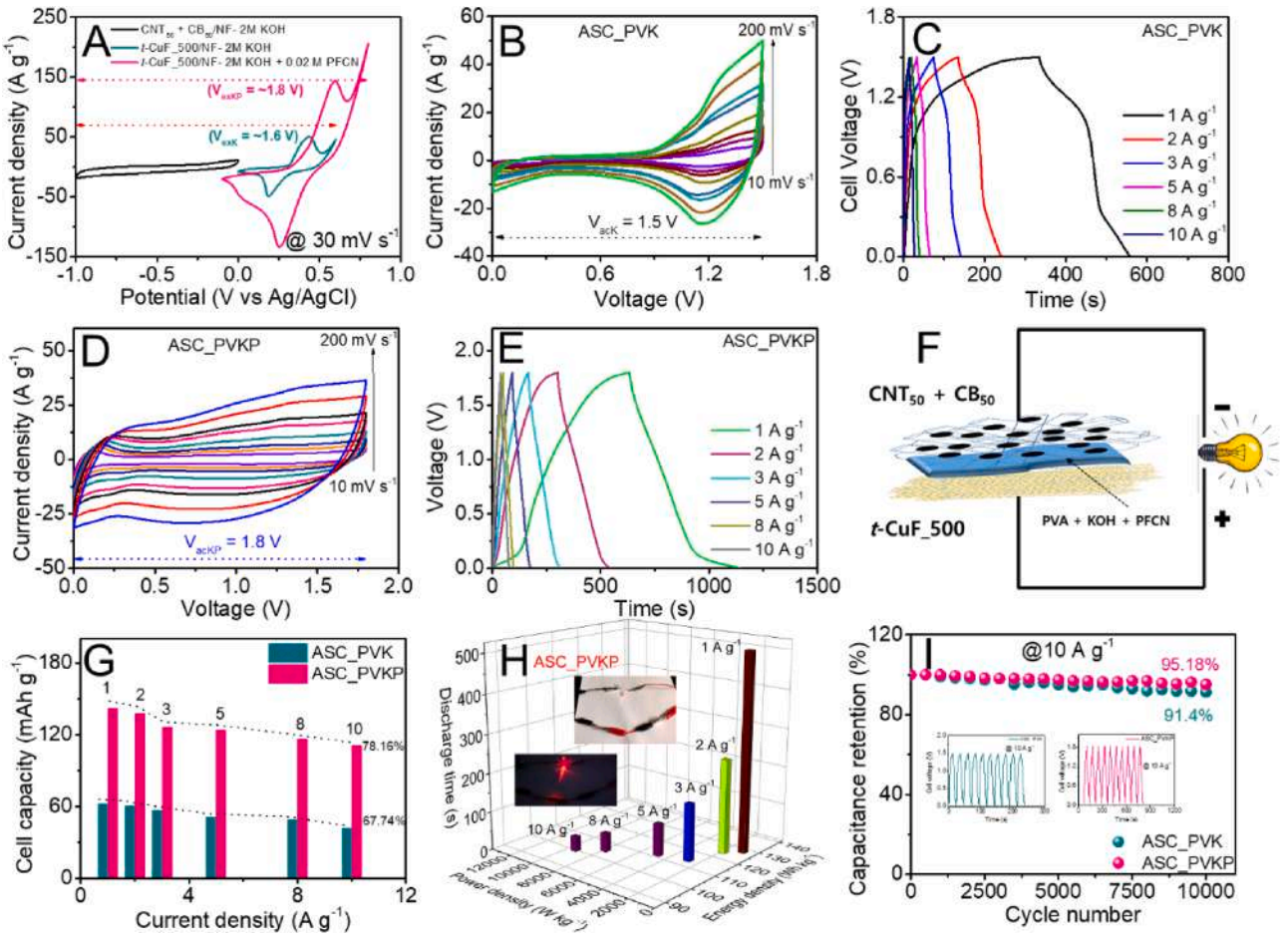

Fig. 6. Asymmetric supercapacitor characterizations; (A) Voltage window comparison of the respective electrodes in different electrolytes @10 mV s^{-1}, (B) CV profiles at various scan rates, (C) CD profiles at various current densities for ASC_PVK, (D) CV profiles at different scan rates, (E) CD profiles at various current densities for ASC_PVKP, (F) a schematic showing the device composition and configuration in redox-gel electrolyte, (G) variation of cell capacity with current densities for ASC_PVK and ASC_PVKP, (H) Ragone bar graph for ASC_PVKP (inset: operation of two red LEDs), and (I) cycling performance for both devices @ 10 A g^{-1}. (For interpretation of the references to color in this figure legend, the reader is referred to the web version of this article.)

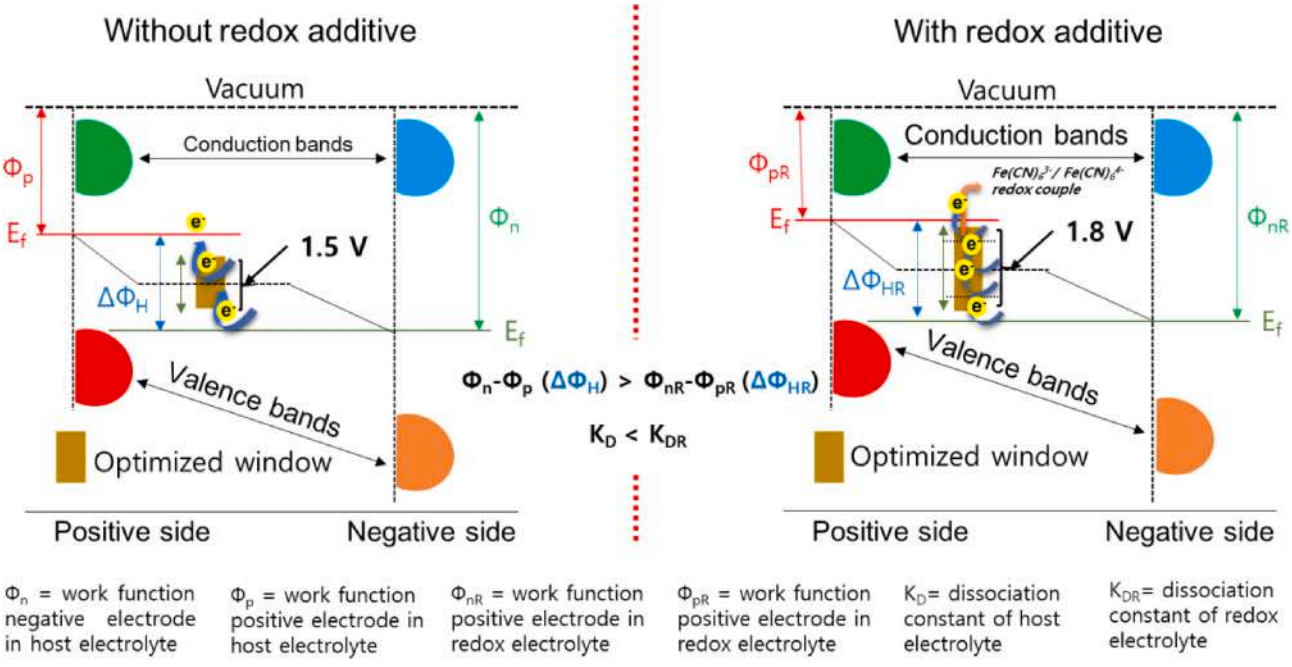

Fig. 7. Schematic representation of the concept involving work function and Fermi energy alteration in the absence and presence of redox additive.

interfacial electrochemistry and thus, the superior performance was achieved.

3.2. Electrochemical performance for water splitting

Additionally, we investigated the electrocatalytic performance of the *t*-CuF_500/NF electrode for OER in alkaline 1 M KOH solution by linear sweep voltammetry at 1 mV s^{-1} and compared it with bare NF and RuO_2/NF electrodes. Fig. 8**A** shows the iR-corrected linear sweep voltammetry (LSV) profiles exhibiting a lower onset potential and higher currents for *t*-Cuf_500/NF than for the other two. Further, the *t*-CuF_500/NF electrode achieved a minimum overpotential (η) of 298 mV at 10 mA cm^{-2}, as shown in Fig. 8**B**. Meanwhile, the *t*-CuF_500/NF electrode also showed the lowest Tafel slope of ~ 57 mV dec^{-1} (Fig. 8**C**), representing favorable and effective OER kinetics. The multistep, EIS, LSV (before and after cycling) and stability profiles further displayed the superior and stable performance of the electrodes (see **Fig. S27 and S28**). The comparison of present values with some recently reported novel materials is shown in **Table S8**, where the present material was superior to all.

Alongside for HER, the iR-corrected LSV profiles collected at 1 mV s^{-1} showed the excellent performance by the *t*-CuF_500/NF electrode with a LSV curve in between the Pt/C/NF and bare NF electrodes (see Fig. 8**D**). Fig. 8**E** shows that the observed overpotential values for the electrode was ~ 103 mV at 10 mA cm^{-2}, for t-CuF_500/NF, which was lower than NF and approaching to Pt/C/NF. Fig. 8**F** shows the Tafel slope for all electrodes depicting the ~ 104 mV dec^{-1} value for *t*-CuF_500/NF lying in between the other two. The lower Tafel slope for *t*-CuF_500 super-architectures proved their unquestionable effectiveness for HER too. The multistep, stability, and EIS profiles further proved the stable performance for HER (see **Fig. S29**). The current HER results were superior to those for various recently reported materials, as listed in **Table S9**. Among bare oxides, such results have been rarely reported until now in water splitting reactions.

The performance of a symmetric *t*-CuF_500 based device was evaluated against a RuO_2/NF||Pt/C/NF based device. **Fig.8**G shows the comparative LSV profiles, at 1 mV s^{-1}, for both devices; the onset potential, at 10 mA cm^{-2}, for a *t*-CuF_500 based device was ~ 1.62 V, which was nearly approaching that of the noble electrocatalysts i.e. the RuO_2/NF||Pt/C/NF based device (~1.58 V). The inset in Fig. 8**G** shows the mechanism taking place at the electrodes surface. Moreover, the current onset potential value was non-dubiously superior to various other similar materials, as visible from Fig. 8**H** (listed in **Table S10**). The stability profile shown in Fig. 8**I** also proved the excellent stability of the device, which was found to be stable for > 30 h, whereas the noble-catalyst-based device was a little degraded within the same time frame. The phase and composition intactness of the material post measurement was confirmed using XPS analysis as shown in **Fig. S30**, which

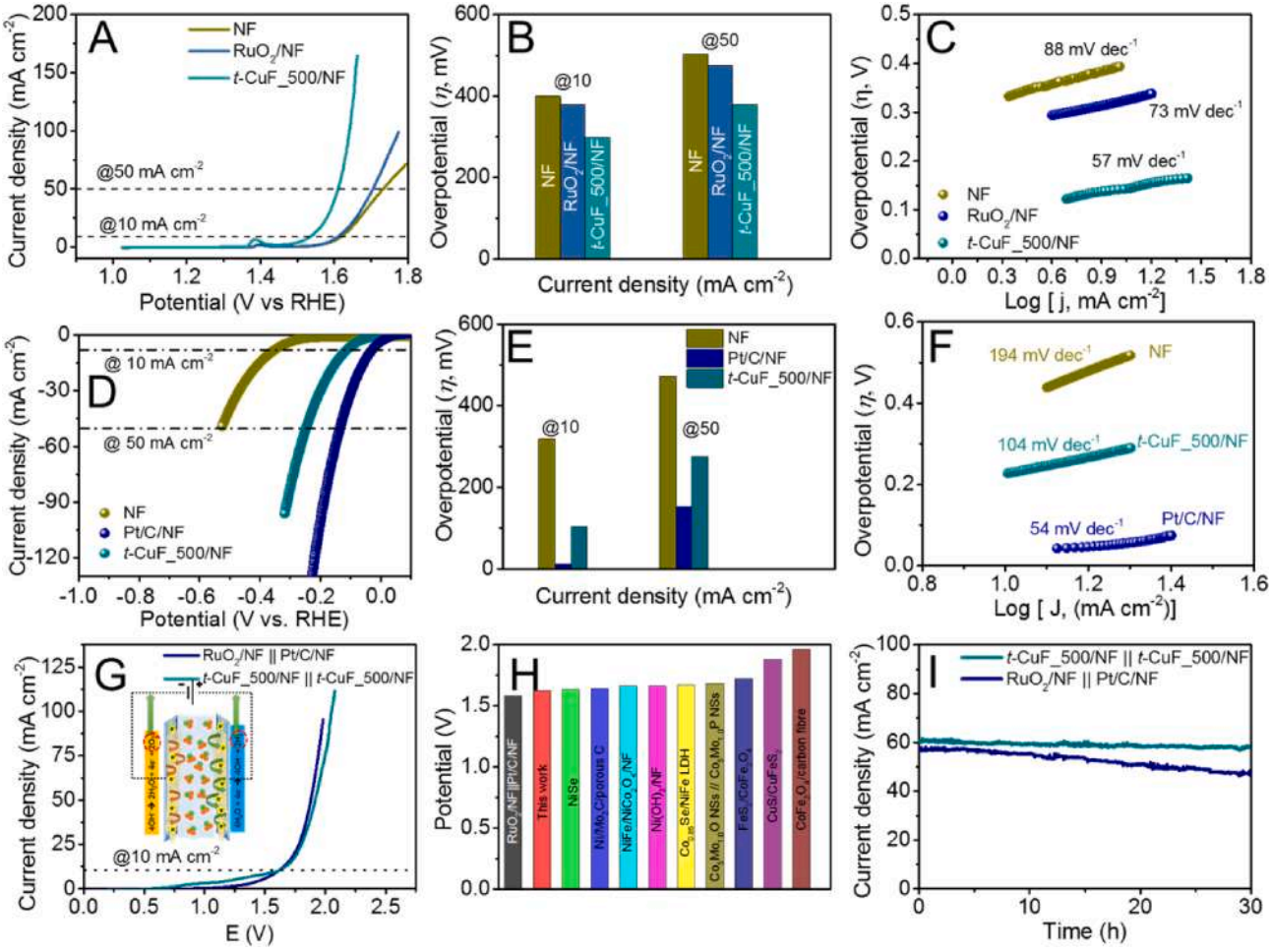

Fig. 8. Water splitting results. (A) OER activity exhibited by LSV profiles, (B) overpotential values comparison @10 and 50 mA cm^{-2}, (C) Tafel plots for NF, RuO_2/NF and *t*-CuF_500/NF electrodes, (D) HER activity showing LSV profiles, (E) overpotential values comparison @10 and 50 mA cm^{-2}, (F) Tafel plots for NF, Pt/C/NF and *t*-CuF_500/NF electrodes, (G) LSV profiles of a symmetric device (*t*-CuF_500/NF|| *t*-CuF_500/NF) and an asymmetric device (RuO_2/NF||Pt/C/NF), where inset shows a schematic for the mechanism taking place at respective electrodes (H) comparison of present cell voltages with other recently reported work, and (I) stability curves for the devices for 30 h @50 mA cm^{-2}.

proved that the elemental composition and their respective intensities remains nearly similar with no discernible degradation.

4. Conclusion

In summary, rationally designed *t*-$CuFe_2O_4$ super-architectures exhibited a tremendous specific surface area of ~ 166 m^2 g^{-1}. As an electrode, *t*-CuF_500 exhibited a maximum specific capacity of ~ 157 mAh g^{-1}, which was much higher than that of the other two in 2 M KOH. Further, the specific capacity was nearly tripled to ~ 450 mAh g^{-1} with the addition of 0.02 M PFCN in 2 M KOH. The as-fabricated solid-state asymmetric supercapacitors in redox-gel electrolyte exhibited a path-breaking ~ 128 Wh kg^{-1} energy density with a broad potential window of ~ 1.8 V at 1 A g^{-1}. In water splitting, the super-architecture displayed superior electrocatalytic performances toward OER (η_{10} ~ 298 mV) and HER (η_{10} ~ 103 mV). Moreover, for full cell, ~1.62 V cell voltage was achieved at 10 mA·cm^{-2} with promising stability for > 30 h (operated at 50 mA·cm^{-2}). The observed results were compared with various recently published results and were found superior for both supercapacitors and water splitting applications. The ultrahigh surface area, good surface porosity, and layered structure suggested that the novel *t*-CuF_500 could be an excellent novel material for next-generation pilot-scale energy storage and conversion systems.

Declaration of Competing Interest

The authors declare that they have no known competing financial interests or personal relationships that could have appeared to influence the work reported in this paper.

Acknowledgements

VS gratefully acknowledges the assistance provided by Mr. Sung Jae Kim for the XPS and TGA measurements. The authors gratefully acknowledge the funding support provided by the Nano-Material Technology Development Program (2016M3A7B4900117) and the Regional Leading Research Center Program (2019R1A5A8080326) through the National Research Foundation supported by the Ministry of Science and ICT of Republic of Korea.

Appendix A. Supplementary data

Supplementary data to this article can be found online at https://doi.org/10.1016/j.cej.2020.127779.

References

[1] X. Li, X. Hao, A. Abudula, G. Guan, Nanostructured catalysts for electrochemical water splitting: current state and prospects, J. Mater. Chem. A 4 (2016) 11973–12000.
[2] Y. Shao, M.F. El-Kady, J. Sun, Y. Li, Q. Zhang, M. Zhu, H. Wang, B. Dunn, R. B. Kaner, Design and mechanisms of asymmetric supercapacitors, Chem. Rev. 118 (2018) 9233–9280.
[3] C. Costentin, T.R. Porter, J.M. Saveant, How do pseudocapacitors store energy? Theoretical analysis and experimental illustration, ACS Appl. Mater. Interfaces 9 (2017) 8649–8658.
[4] S. Liu, Y. Yin, Y. Shen, K.S. Hui, Y.T. Chun, J.M. Kim, K.N. Hui, L. Zhang, S.C. Jun, Phosphorus regulated cobalt oxide@nitrogen-doped carbon nanowires for flexible quasi-solid-state supercapacitors, Small 16 (2020), e1906458.
[5] J. Balamurugan, T.D. Thanh, N.H. Kim, J.H. Lee, Facile synthesis of 3D hierarchical N-doped graphene nanosheet/cobalt encapsulated carbon nanotubes for high energy density asymmetric supercapacitors, J. Mater. Chem. A 4 (2016) 9555–9565.
[6] K. Gopalsamy, J. Balamurugan, T.D. Thanh, N.H. Kim, J.H. Lee, Fabrication of nitrogen and sulfur co-doped graphene nanoribbons with porous architecture for high-performance supercapacitors, Chem. Eng. J. 312 (2017) 180–190.
[7] M. Guo, J. Balamurugan, X. Li, N.H. Kim, J.H. Lee, Hierarchical 3D cobalt-doped Fe_3O_4 nanospheres@NG hybrid as an advanced anode material for high-performance asymmetric supercapacitors, Small 13 (2017) 1701275.
[8] J. Yan, L. Miao, H. Duan, D. Zhu, Y. Lv, W. Xiong, L. Li, L. Gan, M. Liu, Core-shell hierarchical porous carbon spheres with N/O doping for efficient energy storage, Electrochim. Acta 358 (2020), 136899.
[9] Z. Song, H. Duan, L. Miao, L. Ruhlmann, Y. Lv, W. Xiong, D. Zhu, L. Li, L. Gan, M. Liu, Carbon hydrangeas with typical ionic liquid matched pores for advanced supercapacitors, Carbon 168 (2020) 499–507.
[10] L. Miao, Z. Song, D. Zhu, L. Li, L. Gan, M. Liu, Recent advances in carbon-based supercapacitors, Mater. Adv. 1 (2020) 945–966.
[11] L. Miao, X. Qian, D. Zhu, T. Chen, G. Ping, Y. Lv, W. Xiong, Y. Liu, L. Gan, M. Liu, From interpenetrating polymer networks to hierarchical porous carbons for advanced supercapacitor electrodes, Chin. Chem. Lett. 30 (2019) 1445–1449.
[12] M. Jana, S. Saha, P. Khanra, N.C. Murmu, S.K. Srivastava, T. Kuila, J.H. Lee, Bio-reduction of graphene oxide using drained water from soaked mung beans (Phaseolus aureus L.) and its application as energy storage electrode material, Mater. Sci. Eng. B 186 (2014) 33–40.
[13] Y. Tan, H. Wang, P. Liu, Y. Shen, C. Cheng, A. Hirata, T. Fujita, Z. Tang, M. Chen, Versatile nanoporous bimetallic phosphides towards electrochemical water splitting, Energy Environ. Sci. 9 (2016) 2257–2261.
[14] F. Qin, Z. Zhao, M.K. Alam, Y. Ni, F. Robles-Hernandez, L. Yu, S. Chen, Z. Ren, Z. Wang, J. Bao, Trimetallic NiFeMo for overall electrochemical water splitting with a low cell voltage, ACS Energy Lett. 3 (2018) 546–554.
[15] W. Wang, M. Xu, X. Xu, W. Zhou, Z. Shao, Perovskite oxide based electrodes for high-performance photoelectrochemical water splitting, Angew. Chem. Int. Ed. Engl. 59 (2020) 136–152.
[16] W. Yang, J.H. Kim, O.S. Hutter, L.J. Phillips, J. Tan, J. Park, H. Lee, J.D. Major, J. S. Lee, J. Moon, Benchmark performance of low-cost Sb_2Se_3 photocathodes for unassisted solar overall water splitting, Nat. Commun. 11 (2020) 861.
[17] L. Wang, X. Duan, X. Liu, J. Gu, R. Si, Y. Qiu, Y. Qiu, D. Shi, F. Chen, X. Sun, J. Lin, J. Sun, Atomically dispersed Mo supported on metallic Co_9S_8 nanoflakes as an advanced noble-metal-free bifunctional water splitting catalyst working in universal pH conditions, Adv. Energy Mater. 10 (2019) 1903137.
[18] Y. Guo, J. Tang, J. Henzie, B. Jiang, W. Xia, T. Chen, Y. Bando, Y.M. Kang, M.S. A. Hossain, Y. Sugahara, Y. Yamauchi, Mesoporous iron-doped MoS_2/$CoMo_2S_4$ heterostructures through organic-metal cooperative interactions on spherical micelles for electrochemical water splitting, ACS Nano 14 (2020) 4141–4152.
[19] S. Gupta, M.K. Patel, A. Miotello, N. Patel, Metal boride-based catalysts for electrochemical water-splitting: A review, Adv. Funct. Mater. 30 (2019) 1906481.
[20] K. Raju, H. Han, D.B. Velusamy, Q. Jiang, H. Yang, F.P. Nkosi, N. Palaniyandy, K. Makgopa, Z. Bo, K.I. Ozoemena, Rational design of 2D manganese phosphate hydrate nanosheets as pseudocapacitive electrodes, ACS Energy Lett. 5 (2019) 23–30.
[21] S. Prabhakaran, J. Balamurugan, N.H. Kim, J.H. Lee, Hierarchical 3D oxygenated cobalt molybdenum selenide nanosheets as robust trifunctional catalyst for water splitting and zinc-air batteries, Small 16 (2020), e2000797.
[22] J.B. Goodenough, Perspective on engineering transition-metal oxides, Chem. Mater. 26 (2013) 820–829.
[23] M.-S. Balogun, Y. Huang, W. Qiu, H. Yang, H. Ji, Y. Tong, Updates on the development of nanostructured transition metal nitrides for electrochemical energy storage and water splitting, Mater. Today 20 (2017) 425–451.
[24] V. Sharma, I. Singh, A. Chandra, Origin of superior catalytic activity in copper (II) oxide nanoflakes in comparison to solid or even hollow particles, Mater. Lett. 211 (2018) 285–288.
[25] G. Zhang, X. Xiao, B. Li, P. Gu, H. Xue, H. Pang, Transition metal oxides with one-dimensional/one-dimensional-analogue nanostructures for advanced supercapacitors, J. Mater. Chem. A 5 (2017) 8155–8186.
[26] S. Hao, L. Chen, C. Yu, B. Yang, Z. Li, Y. Hou, L. Lei, X. Zhang, NiCoMo hydroxide nanosheet arrays synthesized via chloride corrosion for overall water splitting, ACS Energy Lett. 4 (2019) 952–959.
[27] V. Sharma, I. Singh, A. Chandra, Hollow nanostructures of metal oxides as next generation electrode materials for supercapacitors, Sci. Rep. 8 (2018) 1307.
[28] D.T. Tran, H.T. Le, T.L. Luyen Doan, N.H. Kim, J.H. Lee, Pt nanodots monolayer modified mesoporous Cu@Cu_xO nanowires for improved overall water splitting reactivity, Nano Energy 59 (2019) 216–228.
[29] K.R. Shrestha, S. Kandula, G. Rajeshkhanna, M. Srivastava, N.H. Kim, J.H. Lee, An advanced sandwich-type architecture of $MnCo_2O_4$@N–C@MnO_2 as an efficient electrode material for a high-energy density hybrid asymmetric solid-state supercapacitor, J. Mater. Chem. A 6 (2018) 24509–24522.
[30] L. Wang, D.C. Bock, J. Li, E.A. Stach, A.C. Marschilok, K.J. Takeuchi, E.S. Takeuchi, Synthesis and characterization of $CuFe_2O_4$ nano/submicron wire-carbon nanotube composites as binder-free anodes for Li-ion batteries, ACS Appl. Mater. Interfaces 10 (2018) 8770–8785.
[31] A.M. Balagurov, I.A. Bobrikov, M.S. Maschenko, D. Sangaa, V.G. Simkin, Structural phase transition in $CuFe_2O_4$ spinel, Crystallogr. Rep. 58 (2013) 710–717.
[32] Y. Tang, K. Shih, C. Liu, C. Liao, Cubic and tetragonal ferrite crystal structures for copper ion immobilization in an iron-rich ceramic matrix, RSC Adv. 6 (2016) 28579–28585.
[33] F. Caddeo, D. Loche, M.F. Casula, A. Corrias, Evidence of a cubic iron sub-lattice in t-$CuFe_2O_4$ demonstrated by X-ray absorption fine structure, Sci. Rep. 8 (2018) 797.
[34] A. Bhardwaj, A. Kumar, U. Sim, H.-N. Im, S.-J. Song, Synergistic enhancement in the sensing performance of a mixed-potential NH_3 sensor using SnO_2@$CuFe_2O_4$ sensing electrode, Sensor Actuat. B-Chem. 308 (2020), 127748.
[35] S. Alipoori, S. Mazinani, S.H. Aboutalebi, F. Sharif, Review of PVA-based gel polymer electrolytes in flexible solid-state supercapacitors: Opportunities and challenges, J. Energy Storage 27 (2020), 101072.
[36] J. Balamurugan, T.T. Nguyen, V. Aravindan, N.H. Kim, J.H. Lee, Highly reversible water splitting cell building from hierarchical 3D nickel manganese oxyphosphide nanosheets, Nano Energy 69 (2020), 104432.

[37] J. Balamurugan, T.T. Nguyen, V. Aravindan, N.H. Kim, S.H. Lee, J.H. Lee, All ternary metal selenide nanostructures for high energy flexible charge storage devices, Nano Energy 65 (2019), 103999.
[38] J. Kurian, M.J. Mathew, Structural, optical and magnetic studies of $CuFe_2O_4$, $MgFe_2O_4$ and $ZnFe_2O_4$ nanoparticles prepared by hydrothermal/solvothermal method, J. Magn. Magn. Mater. 451 (2018) 121–130.
[39] X. Dong, B. Ren, Z. Sun, C. Li, X. Zhang, M. Kong, S. Zheng, D.D. Dionysiou, Monodispersed $CuFe_2O_4$ nanoparticles anchored on natural kaolinite as highly efficient peroxymonosulfate catalyst for bisphenol A degradation, Appl. Catal. B-Environ. 253 (2019) 206–217.
[40] J.R. Shimpi, D.S. Sidhaye, B.L.V. Prasad, Digestive ripening: A fine chemical machining process on the nanoscale, Langmuir 33 (2017) 9491–9507.
[41] M. Zhu, D. Meng, C. Wang, G. Diao, Facile fabrication of hierarchically porous $CuFe_2O_4$ nanospheres with enhanced capacitance property, ACS Appl. Mater. Interfaces 5 (2013) 6030–6037.
[42] D. Sarkar, D. Das, S. Das, A. Kumar, S. Patil, K.K. Nanda, D.D. Sarma, A. Shukla, Expanding interlayer spacing in MoS_2 for realizing an advanced supercapacitor, ACS Energy Lett. 4 (2019) 1602–1609.
[43] M.T. Greiner, L. Chai, M.G. Helander, W.-M. Tang, Z.-H. Lu, Transition metal oxide work functions: The influence of cation oxidation state and oxygen vacancies, Adv. Funct. Mater. 22 (2012) 4557–4568.
[44] A. Singh, A. Chandra, Enhancing specific energy and power in asymmetric supercapacitors - A synergetic strategy based on the use of redox additive electrolytes, Sci. Rep. 6 (2016) 25793.